Journal of Sound and Vibration (2000) **234**(5), 737–759
doi:10.1006/jsvi.1999.2898, available online at http://www.idealibrary.com on IDEAL®

NARROWBAND NOISE ATTENUATION CHARACTERISTICS OF IN-DUCT ACOUSTIC SCREENS

MINHONG RIM AND YANG-HANN KIM

Center for Noise and Vibration Control, Department of Mechanical Engineering, Korea Advanced Institute of Science and Technology, Science Town, Taejon 305-701, *South Korea*

(*Received* 26 *January* 1998, *and in final form* 2 *July* 1999)

Noise attenuation characteristics of acoustic screens installed in a straight section of a rectangular duct is studied. It was observed that sound path asymmetry—which arises when an acoustic screen is installed so as to divide the original duct into two asymmetric channels and recombine—gives rise to large narrowband sound attenuation. At first glance, the observed phenomenon looked like it could be explained in terms of the noise cancellation mechanism in Herschel–Quinke tubes, which can be described mathematically by a plane wave model. However, extensive experimental and numerical analyses by the present authors suggested that the narrowband noise attenuation due to sound path asymmetry involves significant higher order mode contributions, hence cannot be described in terms of the plane wave model. Hence, an analytical model that can accurately describe the noise rejection phenomenon was developed. It was found that the higher modes although non-propagating are absolutely necessary to describe the narrowband noise attenuation phenomenon due to sound path asymmetry, which would not have been predicted by a plane wave model.

1. INTRODUCTION

Rectangular ducts are widely used in ventilation systems. The noise emission problem from these systems has recently received a lot of attention as the demand for quieter environment has increased. Commonly used means of noise control in ducts are the Helmholtz resonators and lined expansion chambers, but these devices have inherent disadvantages of taking up excessive space which makes them inappropriate for installation where strict spatial restriction is imposed. This limitation naturally leads one to consider an in-duct acoustic screen that can serve as a reactive noise control device (see Figure 1). Cabelli [1] studied the effect of placing a turning vane in a curved section of a duct which resulted in a significant attenuation of the sound which is transmitted around the bend. Fuller and Bies [2] did a theoretical analysis on turning vanes, but the effect of placing a screen in a straight section of a duct does not seem to be available in literature.

In this paper, the reactive noise attenuation characteristics of the in-duct acoustic screens is studied and their applicability as an alternative means of transmission noise reduction is investigated. Through extensive experiments on the noise attenuation performances of various screens with different shape and geometrical orientation in the duct, a very interesting phenomenon was observed. It was found that when an acoustic screen is installed so as to split the original duct into two asymmetric paths, large narrowband sound attenuation is attained. Initially, the present authors attempted to explain the observed

0022-460X/00/300737 + 23 $35.00/0

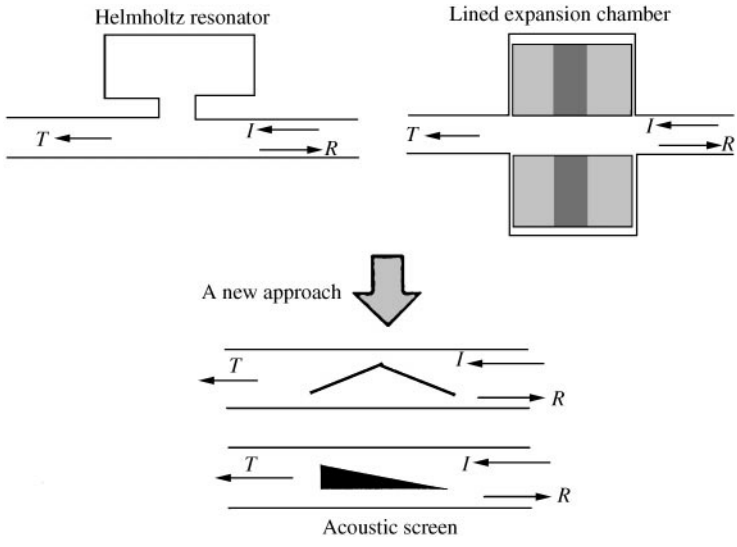

Figure 1. An alternative acoustic attenuator. *I*: Incident wave, *R*: reflected wave, *T*: transmitted wave.

phenomenon in the context of Herschel–Quincke tube noise rejection mechanism, which can be explained by a simple plane wave model. The Herschel–Quincke tube has been studied by various authors in the past [3, 4]. A more general expression for the transmission loss characteristics of the Herschel–Quincke tube was developed by Selamet *et al.* [5] and more recently, creative applications of the tube was studied by Zhi *et al.* [6]. The mathematical analyses for the Herschel–Quincke tubes carried out in the papers aforementioned are based on one-dimensional wave model, and they represented the actual noise rejection phenomena very well. However, extensive experimental studies, including visualization of scattered sound fields on the noise rejection characteristics of the in-duct acoustic screens revealed that one-dimensional plane wave model is insufficient to describe the noise attenuation mechanism of interest in this paper. Higher order modes were found to play an essential role in the noise rejection mechanism due to path asymmetry. The main objective of this paper is the development of an analytical model that accurately describes the physical phenomena involved in the narrowband noise attenuation, and to give a clear physical explanation as to why such acoustical behavior occurs.

2. MEASUREMENT OF TRANSMISSION LOSS

The transmitted noise attenuation performance of an acoustic screen can be assessed quantitatively by the measurement of transmission loss due to its installation in a duct. As a preliminary experimental investigation, the transmission loss was measured for a number of screens with different geometries. The acoustic screens under study were made of rigid steel, so that coupling between sound and screen elements could be neglected. The position of the screens were varied to see its effect on the transmission loss.

2.1. EXPERIMENTAL APPARATUS AND METHOD FOR TL MEASUREMENT

The experimental set-up is shown in Figure 2. A rectangular duct with a cross-sectional dimension of 9 cm $\times$ 10 cm was used, which gives a cut-on frequency of 1715 Hz below

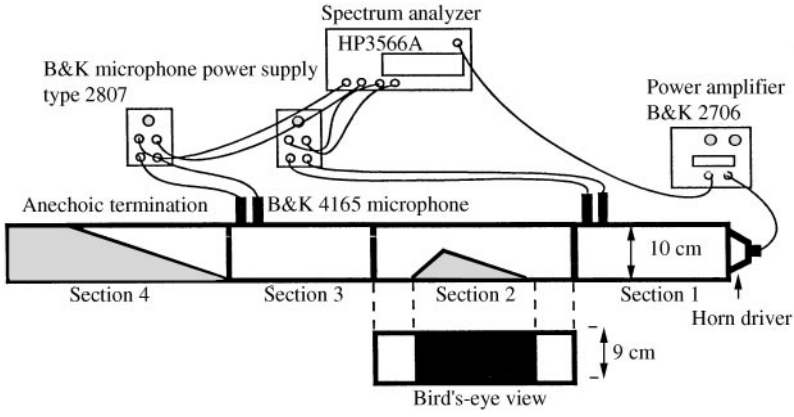

Figure 2. A sketch of the experimental set-up. From the bird's eye view, note that the system can be considered as two-dimensional in the plane wave region. Section 1: 40 cm, Section 2: 50 cm, Section 3: 40 cm, Section 4: 50 cm.

which only the plane wave is propagated. The frequency region of interest is confined to the plane wave region. To give anechoic termination condition at the end of the duct, a 50 cm long wedge made of glass wool was placed at the end of the duct to give a gradual change in impedance, thereby minimizing the reflection from the end of the duct. A test on the performance of the anechoic termination showed power reflection coefficient of less than 0·01 for the frequencies above the cut-off frequency of 250 Hz. The two-microphone method [7] was implemented to measure the transmission loss due to the installation of an acoustic screen in the duct. The microphone spacing was chosen to be 3 cm which is more than adequate for the decomposition of the incident and the reflected waves up to 1715 Hz at which the first cross mode is cut on. Note that the system shown in Figure 2 can be considered as two dimensional in the plane wave region due to the symmetric boundary conditions when viewed from above.

The most difficult decision that had to be made in the experimental study was the choice of acoustic screen shapes. In fact, there would be infinite possibilities for the shape of acoustic screens, but in practice one also has to consider manufacturing cost as well as the noise reduction performances. Therefore, transmission loss for screens with very simple geometries were studied as shown in Figure 5. Once the screen shape is fixed, there are three geometrical variables that determine the size of the screen and its position in the duct. They are the length L, height h, and elevation from the bottom of the duct y as shown in Figure 3. The height of the screen h was fixed at 5 cm in all cases. The range of variation for the height h is rather restricted; for example it would be unrealistic to set $h = 9$ cm in a duct with a height of 10 cm where ventilation is an important function, and a screen with $h = 1$ cm would not give a satisfactory noise reduction performance. It seemed reasonable to tentatively keep h fixed at one-half the duct height.

2.2. EXPERIMENTAL RESULTS—THE EFFECT OF SOUND PATHS ASYMMETRY ON TRANSMISSION LOSS

Extensive experimental study on the noise attenuation characteristics of various acoustic screens gave very interesting results. It was observed that when an acoustic screen is placed so as to divide the original duct into two asymmetric paths so that the incident wave is divided into two and recombine, a sharp peak results in the transmission loss (TL) plot. This

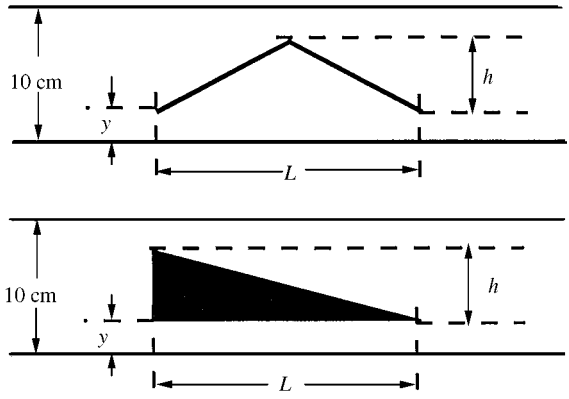

Figure 3. Important geometrical variables. L: Length, h: height, y: elevation from the bottom.

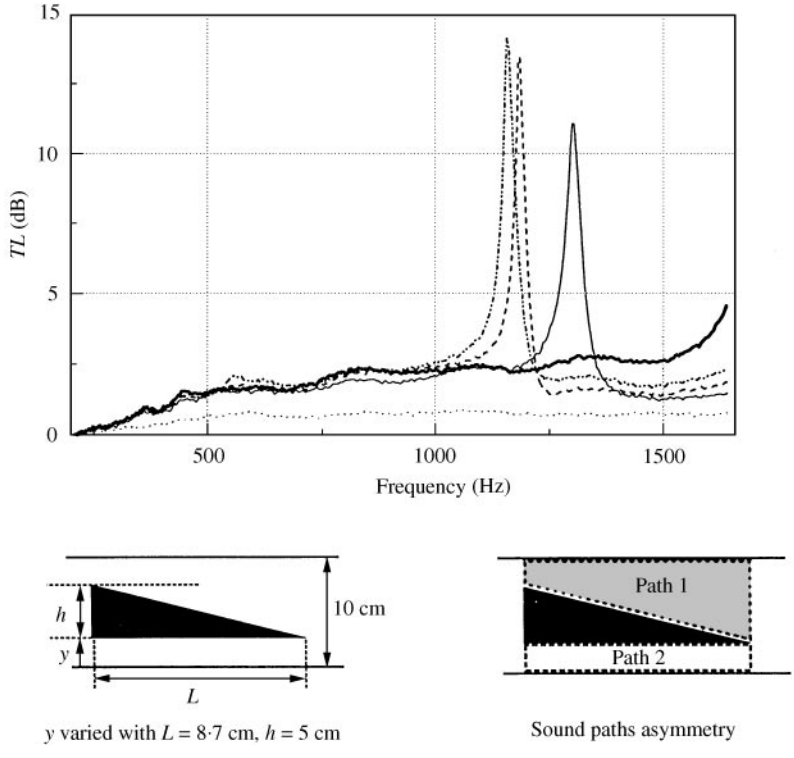

Figure 4. The effect of in-duct screen location on transmission loss: ..... No obstacle; ~~~ $y = 0$; —— $y = 1{\cdot}0$ cm; --------- $y = 2{\cdot}5$ cm; -·-·-·-·-·-·- $y = 4{\cdot}0$ cm.

indicates a large narrowband attenuation of sound power. Figure 4 shows transmission loss for a wedge-shaped screen with the length $L = 8{\cdot}7$ cm. Note that completely different noise attenuation characteristics are observed for the case in which $y = 0$ cm and the cases in which $y \neq 0$. Note that sharp peaks are observed in the TL plot for the $y \neq 0$ cases in which the original duct is split into two asymmetric paths, whereas such behavior is not observed for the case in which $y = 0$ in which only the cross-sectional area is varied along the duct.

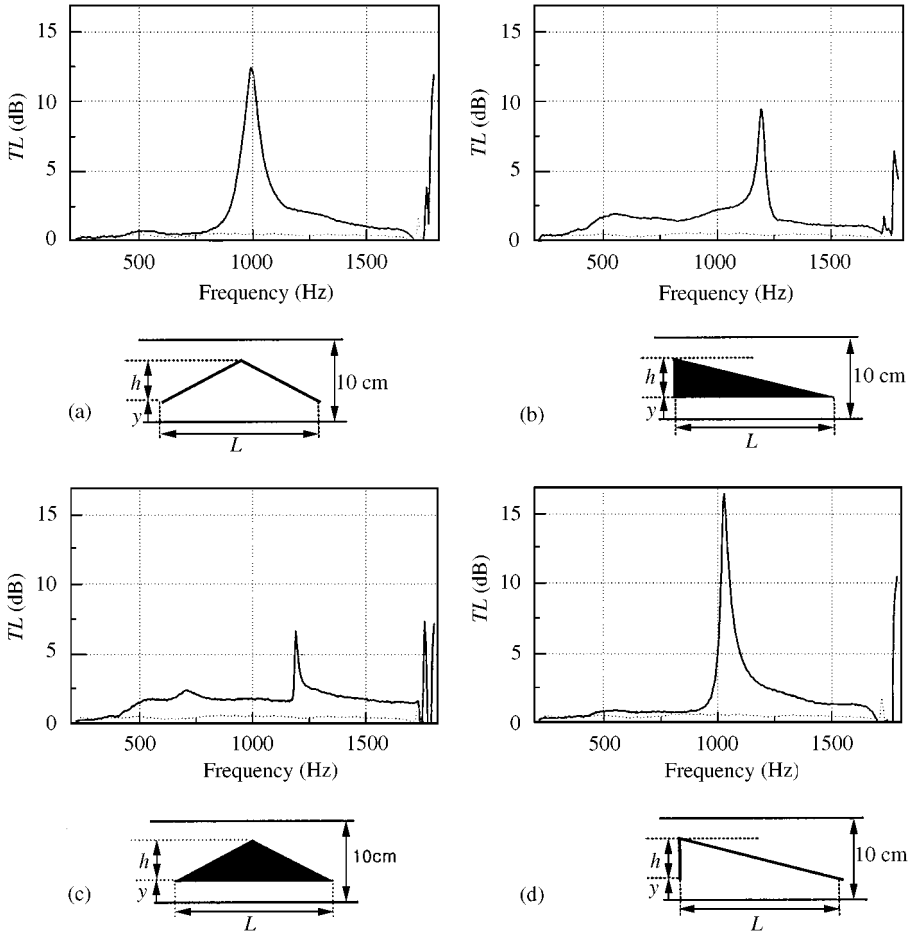

Figure 5. Transmission loss for various acoustic screens. Note that large narrowband sound attenuation is observed in all cases. (a) Shape 1: $L = 10{\cdot}0$ cm, $h = 5$ cm, $y = 2{\cdot}5$ cm. (b) Shape 2: $L = 8{\cdot}7$ cm, $h = 5$ cm, $y = 2{\cdot}5$ cm. (c) Shape 3: $L = 10{\cdot}0$ cm, $h = 5$ cm, $y = 2{\cdot}5$ cm. (d) Shape 4: $L = 8{\cdot}7$ cm, $h = 5$ cm, $y = 2{\cdot}5$ cm.

With these results, the present authors were initially tempted to attribute the narrowband attenuation to noise rejection mechanism in Herschel–Quincke tubes [3]. But, the observed peak transmission loss frequency coincides with neither the type I nor type II peak frequencies given by Selamet *et al* [5]. It seemed to us that the asymmetry in the two divided paths could be responsible for the narrowband noise attenuation phenomena. More experiments were carried out to see if a definite correlation exists between path asymmetry and the narrowband noise attenuation. Figure 5 shows additional experimental results for the cases in which the original duct is split into two asymmetric paths. Note that narrowband noise attenuation is observed in all cases.

From the foregoing observations, a strong correlation was found to exist between the sound paths asymmetry and the narrowband sound attenuation, but the generality of such behavior is yet to be tested. Thus, a logical approach would be to check if similar acoustical behavior would occur if there is a perfect symmetry between the two divided paths. An investigation into the noise attenuation characteristics of a rectangular screen is carried out in the following section. Since it is difficult to implement a perfectly symmetric case

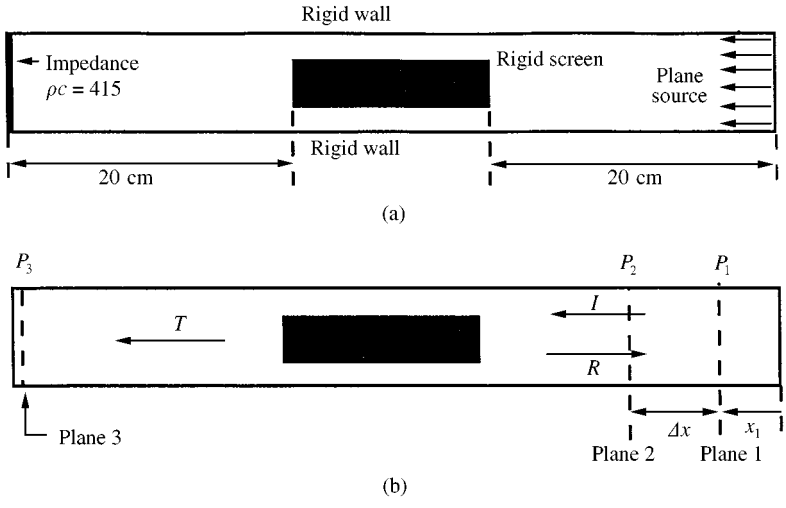

Figure 6. A conceptual sketch of the numerical model. (a) 2D Numerical model for simulation. (b) Explainatory sketch for the computation of TL.

experimentally, numerical method is used to investigate the effect of perfectly symmetric paths division on TL. This would enable us to test the generality of unique acoustical behavior due to the path asymmetry and give us a clue as to why such phenomena occur.

3. NUMERICAL SIMULATION

In order to investigate the effect of perfect sound paths symmetry on noise attenuation, the TL of a rectangular acoustic screen was calculated numerically. A widely used commercial package Sysnoise# was used for the computations: Boundary element method (BEM) was used.

3.1. COMPUTATION OF TRANSMISSION LOSS

To simulate the physical situations implemented in the experiments, a two-dimensional model was used and the boundary conditions were imposed as shown in Figure 6(a). As shown in Figure 6(b), the pressure on Plane 1 can be represented by any point on that plane and it was designated as P_1, since the frequency of interest is confined to the plane wave region. Similarly, P_2 represents the pressure on Plane 2. The transmitted component can be represented by any point on Plane 3 where the anechoic termination condition is imposed. Once, the pressure is calculated on the three planes mentioned, the transmission loss can be calculated.

The pressure at P_1 and P_2 can be expressed in terms of the incident and the reflected components as

$$\hat{P}_1 = \hat{I}e^{-ikx_1} + \hat{R}e^{-ikx_1}, \qquad \hat{P}_2 = \hat{I}e^{-ik(x_1+\Delta x)} + \hat{R}e^{-ik(x_1-\Delta x)}. \tag{1, 2}$$

The superscript ^ designates complex variable. Expressing equations (1) and (2) in matrix form,

$$\begin{bmatrix} \hat{P}_1 \\ \hat{P}_2 \end{bmatrix} = \begin{bmatrix} e^{-ikx_1} & e^{ikx} \\ e^{-ik(x_1+\Delta x)} & e^{ik(x_1-\Delta x)} \end{bmatrix} \begin{bmatrix} \hat{I} \\ \hat{R} \end{bmatrix}, \tag{3}$$

taking the inverse and expressing the incident and the reflected waves in terms of the pressure values representing Planes 1 and 2

$$\begin{bmatrix} \hat{I} \\ \hat{R} \end{bmatrix} = \frac{1}{e^{ik\Delta x} - e^{ik\Delta x}} \begin{bmatrix} e^{ik(x_1+\Delta x)} & -e^{ikx_1} \\ -e^{-ik(x_1+\Delta x)} & e^{-ikx_1} \end{bmatrix} \begin{bmatrix} \hat{P}_1 \\ \hat{P}_2 \end{bmatrix}. \tag{4}$$

Therefore,

$$\hat{I} = \frac{e^{ik(x_1+\Delta x)}\hat{P}_1 - e^{ikx_1}\hat{P}_2}{e^{ik\Delta x} - e^{-ik\Delta x}}, \qquad \hat{R} = \frac{-e^{-ik(x_1+\Delta x)}\hat{P}_1 + e^{-ikx_1}\hat{P}_2}{e^{ik\Delta x} - e^{-ik\Delta x}}. \tag{5, 6}$$

Setting $x_1 = 0$,

$$\hat{I} = \frac{e^{ik\Delta x}\hat{P}_1 - \hat{P}_2}{e^{ik\Delta x} - e^{-ik\Delta x}}. \tag{7}$$

This value represents the pressure of the incident wave from the source. Δx was set equal to 1 cm which is more than enough for the decomposition of the incident and reflected wave in the frequency region of interest. The transmitted wave T can be represented by any point on Plane 3 on which the anechoic termination condition is imposed. The transmission loss can be calculated from the following formula:

$$TL = 20 \log \frac{|\hat{I}|}{|\hat{T}|}. \tag{8}$$

3.2. THE EFFECT OF PERFECTLY SYMMETRIC PATHS DIVISION ON TL

The transmission loss for a rigid rectangular screen with a length of 30 cm and height h of 5 cm was simulated as shown in Figure 7. The first simulation was carried out for the perfectly symmetric case ($y = 2{\cdot}5$ cm) and the second one for an asymmetric case ($y = 1{\cdot}0$ cm). Note that the sound paths asymmetry gives rise to sharp TL peaks in addition to the periodic broadband variation of TL due to the simple change in cross-sectional area, whereas the perfectly symmetric case only shows periodic reflection of the incident sound power just like a simple expansion chamber. Note that a plane wave model would have predicted the same results for both cases. From the foregoing results, it can be concluded that there is a definite link between sound path asymmetry and the large narrowband sound attenuation. At this point, we can only take an educated guess that the reason for the narrowband sound attenuation might be due to the non-uniform impedance distribution at the junctions which could trigger evanescent modes. Further investigation is carried out in the following section in an attempt to understand the narrowband sound attenuation mechanism.

4. MEASUREMENT OF SCATTERED SOUND FIELD

In an attempt to understand the narrowband noise attenuation mechanism, measurements of the scattered sound field induced by path asymmetry were performed. The scattered sound fields were visualized at the maximum transmission loss frequencies.

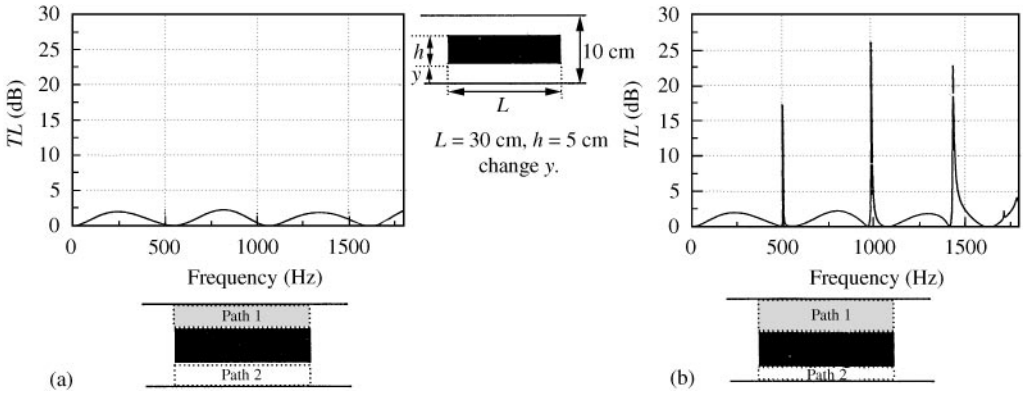

Figure 7. The effect of sound paths asymmetry on transmission loss. (a) Perfectly Symmetric Paths: $y = 2{\cdot}5$ cm. Symmetric Case: $L = 30$ cm, $h = 5$ cm, $y = 2.5$ cm; (b) Asymmetric Paths: $y = 1$ cm. Asymmetric Case: $L = 30$ cm, $h = 5$ cm, $y = 1$ cm.

4.1. EXPERIMENTAL APPARATUS AND METHOD FOR SOUND FIELD MEASUREMENT

The basic structure of experimental set-up remains unchanged from the previous experiments. Section 2 shown in Figure 2 was replaced with a new segment of duct with perforations as shown in Figure 8. Total of 88 holes were perforated with the horizontal spacing of 1·86 cm and the vertical spacing of 1·43 cm. This spatial resolution is enough for accurate measurements of acoustic quantities in the frequency region of interest—the maximum frequency of interest is below 1700 Hz whose wavelength is about 20 cm. The measurement of acoustic quantities on the measurement plane shown in Figure 8 completely describes the acoustic field, since it can be considered as a two-dimensional system due to the symmetric boundary conditions on the duct walls. One may point out that the perforations on the measurement plane could alter the acoustical behavior, however since the step-by-step scanning method—in which all the holes are completely blocked either by microphones or sound sealing materials that simulate rigid wall—is used, the system can be still be considered to be two dimensional. A reference microphone was placed as shown in Figure 8 and four microphones were used to measure the sound pressure. The experiment was carried out for the two cases shown in Figure 9.

4.2. EXPERIMENTAL RESULTS—PHYSICAL INTERPRETATION OF SCATTERED SOUND FIELDS

The pressure plots at the maximum transmission loss frequencies were obtained for the acoustic screens shown in Figure 9. The TL plots for these screens are shown in Figures 5(a) and 5(b). In Figures 10(b) and 10(d), it can be seen that the pressure in two asymmetric paths in both cases are 180° out of phase, and transversal phase variation is observed at the discontinuities which is an indication of the higher order mode generation. Especially, the 1st cross mode seems to be dominant in the very vicinity of the discontinuities. Although the generation of the evanescent modes is well expected, the dominance of the 1st cross deserves special attention, because higher order mode generation is usually negligible in the plane wave region. Resonant behavior is observed in the magnitude plots Figures 10(a) and 10(c). One can see that out-of-phase acoustic modes are formed in two asymmetric paths in both cases. From this information, we can infer that the first cross mode is directly responsible for the out-of-phase standing modes in two asymmetric paths. Also, note that the transversal

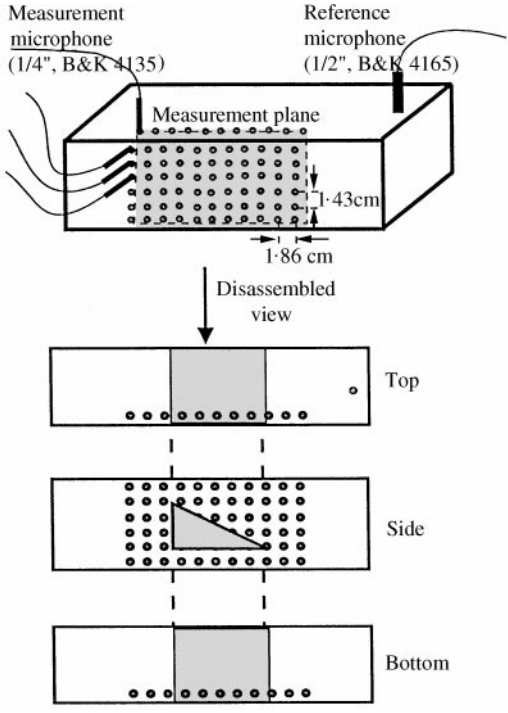

Figure 8. A sketch of experimental set-up for the measurement of scattered sound field.

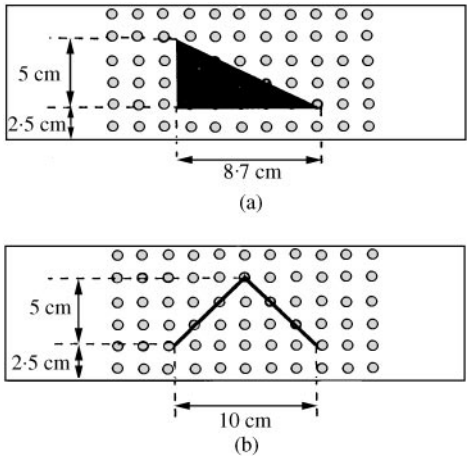

Figure 9. Geometrical arrangements of the screens for the measurement of scattered sound fields.

acoustical interaction is significant and the resonance phenomenon is two dimensional in nature.

From the foregoing observation, it can be concluded that a simple plane wave model cannot describe the acoustical behavior involved in narrowband noise attenuation, although the effect of higher order modes would only be important near the discontinuities.

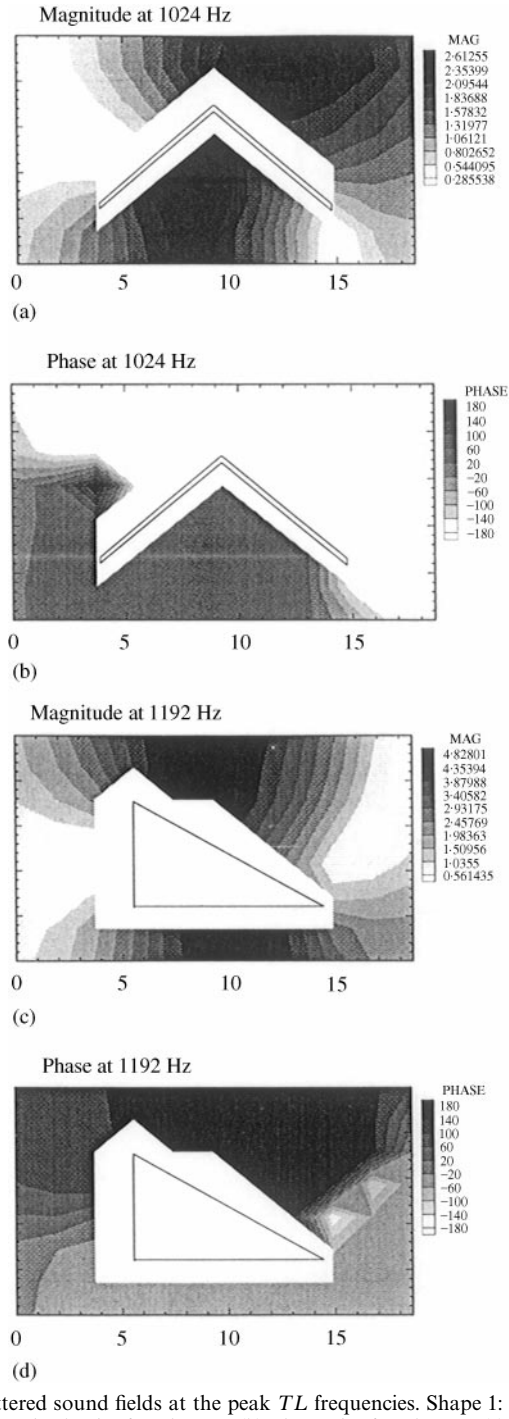

Figure 10. Measured scattered sound fields at the peak TL frequencies. Shape 1: Hat-shaped screen, Shape 2: Wedge-shaped screen. (a) Magnitude plot for Shape 1. (b) Phase plot for Shape 1. (c) Magnitude plot for Shape 2. (d) Phase plot for Shape 2.

It is evident that the evanescent modes are essential in describing the noise attenuation phenomenon. In the following section, an analytical model is developed that can accurately describe the narrowband noise attenuation mechanism.

5. ANALYTICAL MODEL

The visualization of the scattered sound fields at peak TL frequencies revealed that the higher order mode generation at the discontinuities is significant. Especially, it was evident that the 1st cross mode is responsible for producing mutually out-of-phase interference fields in two divided paths. In this section, analytical models which takes account of the higher order mode generation are developed.

5.1. ANALYTICAL MODEL FOR WEDGE-SHAPED SCREEN

The wave propagation in the duct system with a wedge-shaped screen installed can be analyzed by dividing it into four sections as shown in Figure 11. Careful observation of the scattered sound fields at the maximum TL frequencies in Figures 10(c) and 10(d) implies that the transversal phase and magnitude variations within Paths 1 and 2 are negligible, and therefore assuming plane wave propagation in the two divided paths seems reasonable. At each discontinuity an infinite set of higher order modes are generated. Since the frequency range of interest is confined to the plane wave region, the higher order modes will decay and only the plane wave modes will propagate without attenuation. However, the contribution of the higher order modes near the discontinuities is significant at the peak TL frequency as is evident in Figure 10. Due to the non-uniform transversal distribution of impedance at the discontinuities, several modes are likely to be excited by single-mode incident wave. Hence the generation of the higher order modes has to be considered in the reflected and transmitted waves.

The mathematical expression in each section is as follows:

$$I = \hat{P}_0^I \exp[\mathrm{i}(\omega t - k_0 x)], \tag{9}$$

$$R = \sum_{m=0}^{n} \hat{P}_m^R \cos\left(m\pi \frac{y}{H}\right) \exp[\mathrm{i}(\omega t + k_m x)], \tag{10}$$

$$X_1(x,t) = \left\{\hat{C}_1 J_0\left[k_0\left(\frac{W_1 L}{h} - x\right)\right] + \hat{C}_2 Y_0\left[k_0\left(\frac{W_1 L}{h} - x\right)\right]\right\} \exp(\mathrm{i}\omega t), \tag{11}$$

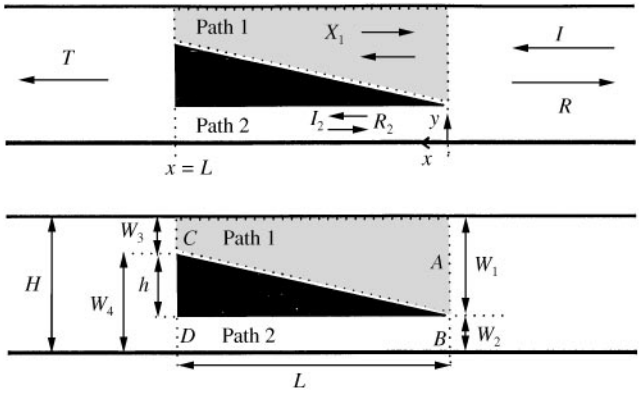

Figure 11. Definition sketch for theoretical analysis of the wedge-shaped screen.

$$I_2 = \hat{I}_2 \exp[\mathrm{i}(\omega t - k_0 x)], \tag{12}$$

$$R_2 = \hat{R}_2 \exp[\mathrm{i}(\omega t + k_0 x)], \tag{13}$$

$$T = \sum_{m=0}^{n} \hat{P}_m^T \cos\left(m\pi \frac{y}{H}\right) \exp[\mathrm{i}(\omega t - k_m x)], \tag{14}$$

where $k_m = k_x = \sqrt{(\omega/c)^2 - (m\pi/H)^2}$ and X_1 describes the sound field in Path 1 (see Figure 11). X_1 is obtained from the Webster Horn equation [8]. (see appendix A for the derivation). In order to satisfy the continuity condition across the interfaces, continuity of acoustic pressure and particle velocity is imposed.

The mean pressure at the junctions A, B, C and D shown in Figure 11 is matched in order to satisfy the pressure continuity conditions.

Pressure continuity at A provides

$$\hat{P}_0^I W_1 + \int_{W_1}^{H} \left\{ \sum_{m=0}^{n} \hat{P}_m^R \cos\left(m\pi \frac{y}{H}\right) \right\} \mathrm{d}y = \hat{C}_1 W_1 J_0\left(\frac{k_0 W_1 L}{2h}\right) + \hat{C}_1 W_1 Y_0\left(\frac{k_0 W_1 L}{2h}\right). \tag{15}$$

Pressure continuity at B provides

$$\hat{P}_0^1 W_1 + \int_{0}^{W_2} \left\{ \sum_{m=0}^{n} \hat{P}_m^R \cos\left(m\pi \frac{y}{H}\right) \right\} \mathrm{d}y = \hat{I}_1 W_2 + \hat{R}_2 W_2. \tag{16}$$

Pressure continuity at C provides

$$\int_{W_4}^{H} \left\{ \sum_{m=0}^{n} \hat{P}_m^T \cos\left(m\pi \frac{y}{H}\right) \exp(-\mathrm{i}k_m L) \right\} \mathrm{d}y = \hat{C}_1 W_3 J_0\left[k_0 L \left(\frac{W_1}{h} - 1\right)\right] + \hat{C}_2 W_3 Y_0\left[k_0 L \left(\frac{W_1}{h} - 1\right)\right]. \tag{17}$$

Pressure continuity at D provides

$$\int_{0}^{W_2} \left\{ \sum_{m=0}^{n} \hat{P}_m^T \cos\left(m\pi \frac{y}{H}\right) \exp(-\mathrm{i}k_m L) \right\} \mathrm{d}y = \hat{I}_2 W_2 \exp(-\mathrm{i}k_0 L) + \hat{R}_2 W_2 \exp(\mathrm{i}k_0 L). \tag{18}$$

Velocity continuity at $x = 0$ provides

$$\hat{P}_0^I - \sum_{m=0}^{n} \left(\frac{k_m}{k_0}\right) \hat{P}_m^R \cos\left(m\pi \frac{y}{H}\right) = \hat{C}_1 \mathrm{i} J_1\left(\frac{k_0 W_1 L}{h}\right) + \hat{C}_2 \mathrm{i} Y_1\left(\frac{k_0 W_1 L}{h}\right), \quad W_2 \leqslant y \leqslant H, \tag{19}$$

$$\hat{P}_0^I - \sum_{m=0}^{n} \left(\frac{k_m}{k_0}\right) \hat{P}_m^R \cos\left(m\pi \frac{y}{H}\right) = \hat{I}_2 - \hat{R}_2, \quad 0 \leqslant y \leqslant W_2. \tag{20}$$

By multiplying both sides of equations (19) and (20) by the eigenfunction $\cos(m\pi\,(y/H))$ and integrating over the interface at $x = 0$, the modal coefficients can be obtained. From the

orthogonality property of eigenfunctions, the following relations can be obtained:

$m = 0$:

$$\hat{P}_0^I H - \hat{P}_0^R H = \hat{C}_1 \mathrm{i} W_1 J_1\left(\frac{k_0 W_1 L}{h}\right) + \hat{C}_2 \mathrm{i} W_i Y_1\left(\frac{k_0 W_1 L}{h}\right) + \hat{I}_2 W_2 - \hat{R}_2 W_2, \tag{21}$$

$m \neq 0$:

$$\begin{aligned} -\left(\frac{k_1}{k_0}\right)\left(\frac{H}{2}\right)\hat{P}_1^R &= \hat{C}_1 \mathrm{i} J_1\left(\frac{k_0 W_1 L}{h}\right)\int_{W_2}^{H} \cos\left(m\pi \frac{y}{H}\right)\mathrm{d}y \\ &\quad + \hat{C}_2 \mathrm{i}\, Y_1\left(\frac{k_0 W_1 L}{h}\right)\int_{W_2}^{H} \cos\left(m\pi \frac{y}{H}\right)\mathrm{d}y \\ &\quad + \hat{I}_2 \int_0^{W_2} \cos\left(m\pi \frac{y}{H}\right)\mathrm{d}y - \hat{R}_2 \int_0^{W_2} \cos\left(m\pi \frac{y}{H}\right)\mathrm{d}y. \end{aligned} \tag{22}$$

Velocity continuity at $x = L$ provides

$$\begin{aligned} &\sum_{m=0}^{n}\left(\frac{k_m}{k_0}\right)\hat{P}_m^T \cos\left(m\pi \frac{y}{H}\right)\exp(-\mathrm{i}k_m L) \\ &\quad = \hat{C}_1 \mathrm{i} J_1\left[k_0\left(\frac{W_1 L}{h} - x\right)\right] + \hat{C}_2 \mathrm{i} Y_1\left[k_0\left(\frac{W_1 L}{h} - 1\right)\right], \quad W_4 \leqslant y \leqslant H, \end{aligned} \tag{23}$$

$$\sum_{m=0}^{n}\left(\frac{k_m}{k_0}\right)\hat{P}_m^T \cos\left(m\pi \frac{y}{H}\right)\exp(-\mathrm{i}k_m L) = 0, \quad W_2 \leqslant y \leqslant W_4, \tag{24}$$

$$\begin{aligned} &\sum_{m=0}^{n}\left(\frac{k_m}{k_0}\right)\hat{P}_m^T \cos\left(m\pi \frac{y}{H}\right)\exp(-\mathrm{i}k_m L) \\ &\quad = \hat{I}_2 \exp(-\mathrm{i}k_0 L) - \hat{R}_2 \exp(\mathrm{i}k_0 L), \quad 0 \leqslant y \leqslant W_2. \end{aligned} \tag{25}$$

By multiplying both sides of equations (23)–(25) by $\cos(m\pi(y/H))$ and integrating over the interface at $x = L$, the modal coefficients can be obtained. From the orthogonality property, the following relations can be obtained:

$m = 0$:

$$\begin{aligned} \hat{P}_0^T H \exp(-\mathrm{i}k_0 \mathrm{L}) &= \hat{C}_1 \mathrm{i} W_3 J_1\left[k_0 L\left(\frac{W_1}{h} - 1\right)\right] + \hat{C}_2 \mathrm{i} W_3 Y_1\left[k_0 L\left(\frac{W_1}{h} - 1\right)\right] \\ &\quad + \hat{I}_2 W_2 \exp(-\mathrm{i}k_0 L) - \hat{R}_2 W_2 \exp(\mathrm{i}k_0 L), \end{aligned} \tag{26}$$

$m \neq 0$:

$$\hat{P}_m^T\left(\frac{k_m}{k_0}\right)\left(\frac{H}{2}\right)\exp(-\mathrm{i}k_mL)$$

$$= \hat{C}_1 \mathrm{i} J_1\left[k_0L\left(\frac{W_1}{h}-1\right)\right]\int_{W_4}^{H}\cos\left(m\pi\frac{y}{H}\right)\mathrm{d}y$$

$$+ \hat{C}_2 \mathrm{i}\, Y_1\left[k_0L\left(\frac{W_1}{h}-1\right)\right]\int_{W_4}^{H}\cos\left(m\pi\frac{y}{H}\right)\mathrm{d}y + \hat{I}_2\exp(-\mathrm{i}k_0L)\int_0^{W_2}\cos\left(m\pi\frac{y}{H}\right)\mathrm{d}y$$

$$- \hat{I}_2\exp(\mathrm{i}k_0L)\int_0^{W_2}\cos\left(m\pi\frac{y}{H}\right)\mathrm{d}y. \tag{27}$$

Now, one can find the unknown coefficients from the relations just derived. The accuracy of the model depends on the number of higher modes considered in the analysis, but a trade-off has to be made between the accuracy and computation effort. Based on the scattered sound fields obtained for the maximum TL frequencies in Figure 10, the number of higher modes to be considered was set equal to two ($n = 2$), so that only the first two cross modes are taken into account in addition to the plane mode in the reflected wave R and transmitted wave T. This truncation is expected to give satisfactory results considering the dominance of the 1st higher order mode at the peak TL frequencies in the scattered sound fields as is evident in Figures 10(b) and 10(d). With $n = 2$, we have 10 equations and 11 unknown coefficients. Setting $\hat{P}_0^I = 10\mathrm{i}$ as a reference value, all the other coefficients can be found. Transmission loss can be calculated from the following equation:

$$TL = 20\log\left|\frac{\hat{P}_0^I}{\hat{P}_0^T}\right|. \tag{28}$$

In order to prove the validity of the assumptions and test the generality of the analytical approach made in this section, additional theoretical analysis was performed. Based on the same assumptions and physical reasoning given in this section, theoretical analysis was also performed for the rectangular screen. Detailed derivations for the rectangular screen is carried out in this section, because the basic approach and assumptions are exactly same as that for the wedge-shaped screen just shown. Only brief descriptions are given in Appendix B.

5.2. VALIDATION OF ANALYTICAL RESULTS

Transmission loss was obtained based on the analytical model. The validity of the analytical model was confirmed by comparing the analytical results with those of the numerical method and experiments. Figure 12 shows the comparisons. The analytical result for the rectangular screen with $L = 30$ cm, $h = 5$ cm, $y = 1$ cm shows very good agreement with the numerical result. The comparison between the analytical and the experimental results in Figure 12 confirms that the analytical model is reliable. Figure 12(a) shows the comparison between the experimental and analytical results for the wedge-shaped screen with $L = 8{\cdot}7$ cm, $h = 5$ cm, $y = 2{\cdot}5$ cm. Note that the peak TL frequency is precisely predicted, but the magnitude of the peak TL shows large deviation from the experimental

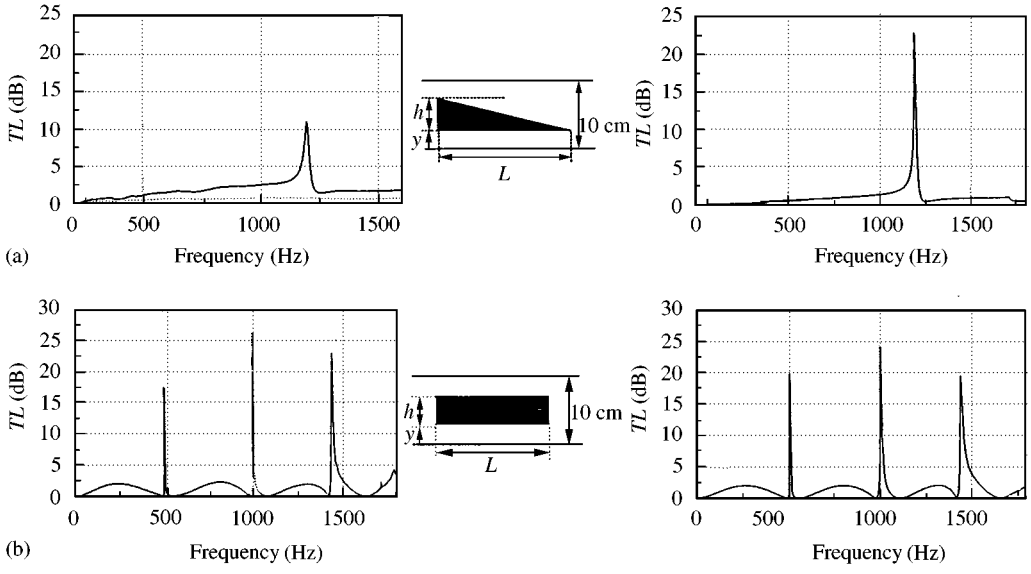

Figure 12. Validity of analytical model. The analytical results show close agreement with the numerical and the experimental results. (a) Experimental versus analytical result for wedge-shaped screen $L = 8{\cdot}7$ cm, $h = 5$ cm, $y = 2{\cdot}5$ cm. Experimental Result: $L = 8{\cdot}7$ cm, $h = 5{\cdot}0$ cm, $y = 2{\cdot}5$ cm; Analytical Model: $L = 8{\cdot}7$ cm, $h = 5$ cm, $y = 2{\cdot}5$ cm; (b) BEM versus analytical results for rectangular screen $L = 30$ cm, $h = 5$ cm, $y = 1$ cm. BEM Result: $L = 30$ cm, $h = 5$ cm, $y = 1$ cm; Analytical Model: $L = 30$ cm, $h = 5$ cm, $y = 1$ cm.

result. The magnitude of the peak TL in the analytical model are overestimated and its bandwidth is slightly narrower than that of the experimental result. These discrepancies are attributed to the neglect of damping effect in the analytical model. From the foregoing results, we can conclude that the basic assumptions for the analytical model are valid and the truncation of the number of higher order modes to two ($n = 2$) proved to be appropriate.

6. PHYSICAL INTERPRETATION AND UNDERSTANDING NARROWBAND SOUND ATTENUATION MECHANISM

Since the analytical model proved to describe the narrowband sound attenuation characteristics very accurately, this model can now be utilized to gain in-depth understanding of the noise reduction mechanism.

Recall that the higher order mode generation at the discontinuities was observed to be what gives rise to narrowband sound attenuation phenomena. Especially, it was evident in the scattered sound fields that the 1st cross made generation is directly responsible for the cancellation of the acoustic energy. Using the analytical model, a quantitative analysis is possible. The contribution of the evanescent modes at the discontinuities is obtained. Figure 13 shows the ratios of the 1st cross mode coefficients P_{r1} at the inlet junction and P_{t1} at the outlet junction against the incident wave coefficient P_{i0}, i.e., P_{r1}/P_{i0} and P_{t1}/P_{i0}, respectively, for the rectangular screen. Note that the contribution of the 1st cross mode is significant at the frequencies where TL peaks, but is almost negligible at other frequencies. It is important to note that the 1st higher order mode contribution is zero in the perfectly symmetric case shown in Figures 13(d) and 13(f). As a result, spiky noise attenuation is not observed in Figure 13(b). From these data, we can infer that the asymmetric transversal

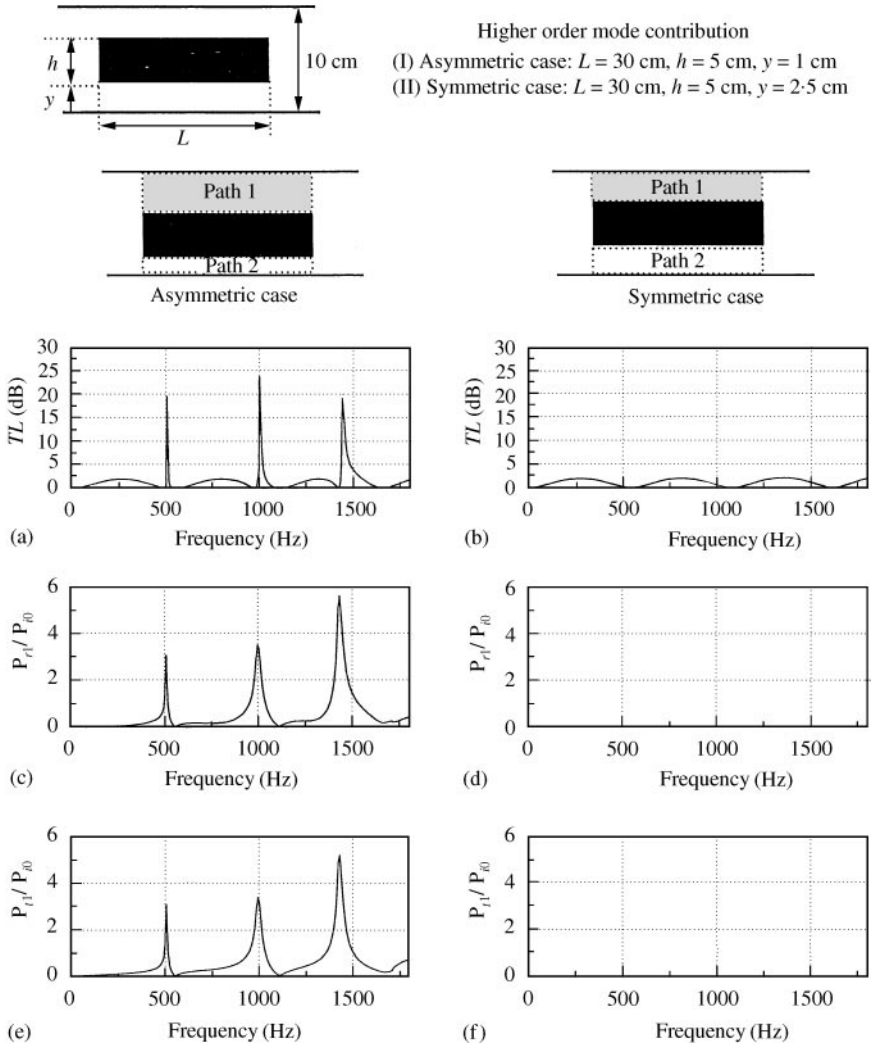

Figure 13. Contribution of 1st higher order mode. (c) and (d) show plots for $\hat{P}_1^R/\hat{P}_0^I$ at the inlet interface. (e) ad (f) show plots for $\hat{P}_1^T/\hat{P}_0^I$ at the outlet interface. Note that the higher order mode contribution is zero for the symmetric case. (a) (I) Asymmetric case: transmission loss; (b) (II) Symmetric case: transmission loss; (c) (I) Asymmetric case: P_{r1}/P_{i0} at the inlet interface; (d) (II) Symmetric case: P_{r1}/P_{i0} at the inlet interface; (e) (I) Asymmetric case: P_{t1}/P_{i0} at the outlet interface; (f) (II) Symmetric case: P_{t1}/P_{i0} at the outlet interface.

impedance distribution at the discontinuities is responsible for the excitation of the 1st cross mode. Since the 1st cross mode is non-propagating in the frequency region of interest, the acoustic energy cannot be transmitted downstream and results in reflection. Unlike the asymmetric cases, perfectly symmetric impedance distribution would not allow the 1st cross mode to be triggered. The important role of the 1st cross mode is what makes the noise rejection due to sound path asymmetry unique. The narrowband noise rejection in Figure 13(a) would not have been predicted at all if the higher order modes had been neglected in the mathematical model.

It is evident that the non-propagating higher order modes play a significant role in the narrowband noise attenuation mechanism when sound paths asymmetry is present. After

careful analyses of the previously obtained results, an interesting pattern which can be a clue for the full understanding of the attenuation mechanism was found. Looking carefully at Figure 7 again, one can notice that the locations of the three sharp peaks in the TL plot for the asymmetric case are almost identical to the locations of the troughs in the TL plot for the symmetric case. The locations of the first two peaks coincide with those of the first two troughs. The third peak shows a slight deviation from the third trough. This is because of the added mass effect induced by the evanescent modes in the very vicinity of the discontinuities. Due to the increase in the effective mass, the third peak is shifted toward the lower frequency region, but correspondence does seem to exist between the third peak and trough. Recall that the troughs in the TL plot correspond to the resonance frequencies at which the length of the screen equals to multiples of one-half a wavelength or $L = n\lambda/2$ ($n = 1, 2, \ldots,$). If this turns out to be a general behavior, then it means the narrowband sound attenuation mechanism can be interpreted as a longitudinal resonance along the two asymmetric paths. In order to see if there is a consistent relationship between the screen length and the wavelengths corresponding to the peak TL frequencies, the pressure distributions along Paths 1 and 2 were obtained at each peak TL frequency for the rectangular screen. Figure 14 shows the theoretically obtained acoustic modes at each peak frequency along Paths 1 and 2. The pressure modes for the wedge-shaped screen is also shown in Figure 15. Results in Figures 14 and 15 suggest that the first peak corresponds to the frequency at which $L_{eff} = \lambda/2$ and the second peak at which $L_{eff} = \lambda$ and so on. Here L_{eff} designates the effective length, perceived by the air particles, which is longer than the actual screen length L due to the added mass effect. It is important to note that the pressure modes in Paths 1 and 2 are out of phase. This is a clear indication that the 1st cross mode generated at the junctions is directly responsible for the formation of out-of-phase interference fields in two asymmetric paths. It has to be added that the effective length might not be so obvious in some cases. When the length of a screen L is long, the effective length of the screen is almost equal to the actual length, but as the length gets shorter the percent deviation of the effective length from the actual length increases as shown in Figures 16(a) and 16(b). The effective length was estimated from $L_{eff} = \lambda_{1st}/2$, where λ_{1st} is wavelength corresponding to the 1st peak TL frequency. Note that the percent deviation is nearly 50% when $L = 10$ cm and decreases as L is increased. The foregoing observations and analyses are compatible with the suggestion that peak TL frequencies correspond to the longitudinal resonance frequencies at which the effective length of a screen equals the multiples of one-half wavelength: $L_{eff} = n\lambda/2$ for $n = 1, 2, 3, \ldots$ One can see a striking similarity between what we suggested and the mathematical expression for the type II transmission loss peaks in the Herschel–Quincke tubes $f_2 = nc_0/(L_1 + L_2)$, $n = 1, 2, \ldots,$ as given by Selamet *et al.* [5]. Note that since the speed of sound $c_0 = f\lambda$, $f_2 = nc_0/(L_1 + L_2)$ is equivalent to $(L_1 + L_2) = n\lambda$. If we let $L_{eff} = (L_1 + L_2)/2$, then the two equations are identical. As is evident in our analyses, the effective length of a screen is not the average of the two asymmetric path lengths, i.e., $L_{eff} \neq (L_1 + L_2)/2$. Hence L_1 and L_2 can be interpreted as the length of Paths 1 and 2 respectively. Although the type II noise rejections in the Herschel–Quincke tubes and those due to path asymmetry can both be interpreted as longitudinal resonance phenomena, the latter cannot be described without including the higher order mode effects. Thus, the plane wave model fails to describe the phenomenon we have observed. By taking account of the higher order modes, the transversal acoustical interaction near the discontinuities could be described in our model, hence the resonance frequency is accurately predicted which would have been missed in a plane wave model. Figures 16(c)–16(f) show the sensitivity of 1st peak TL frequency with respect to y and h. Note that the 1st peak frequency becomes less sensitive to the variation in y as the length L increases. Also, note that peak location is almost independent of the

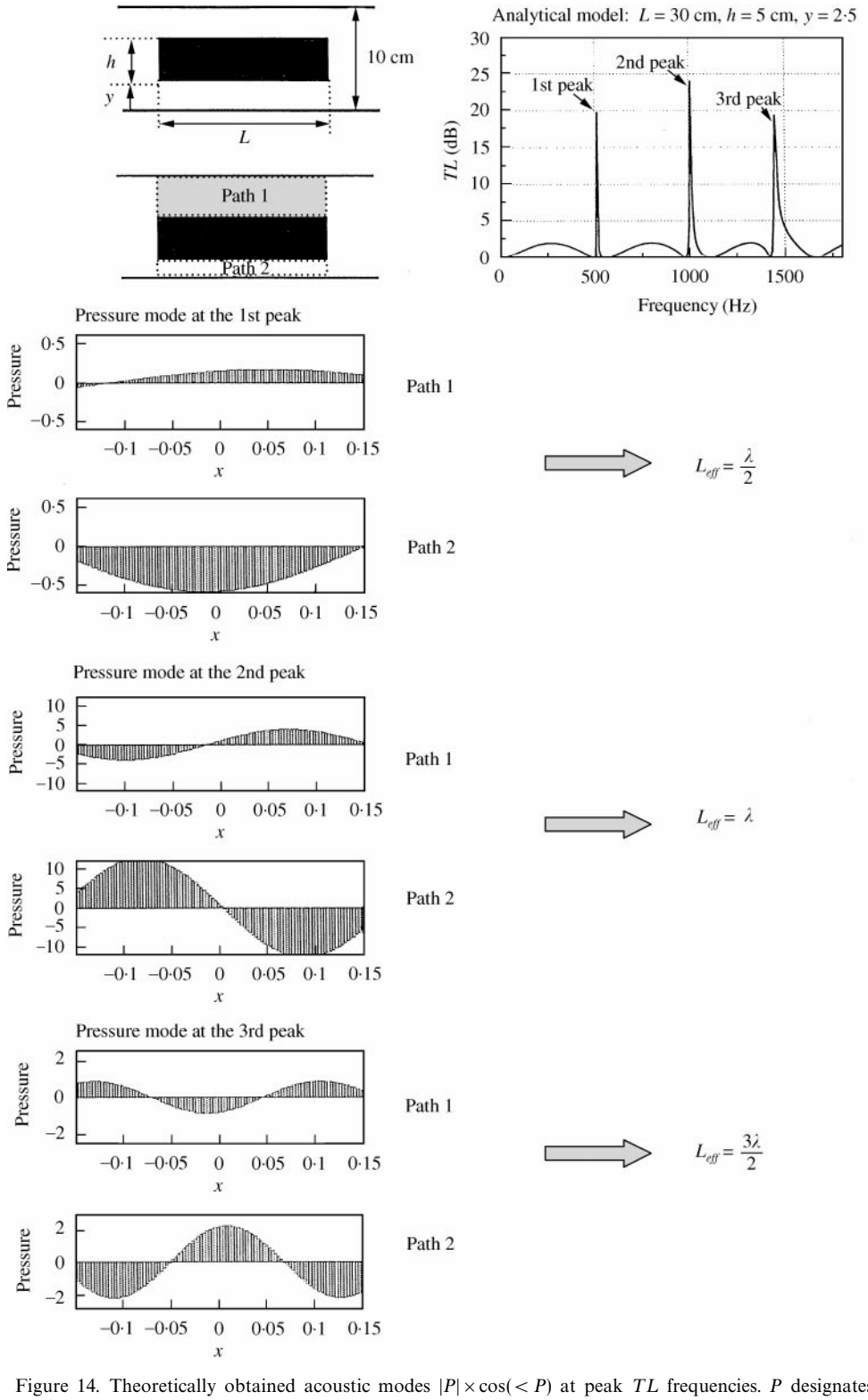

Figure 14. Theoretically obtained acoustic modes $|P| \times \cos(< P)$ at peak TL frequencies. P designates the acoustic pressure.

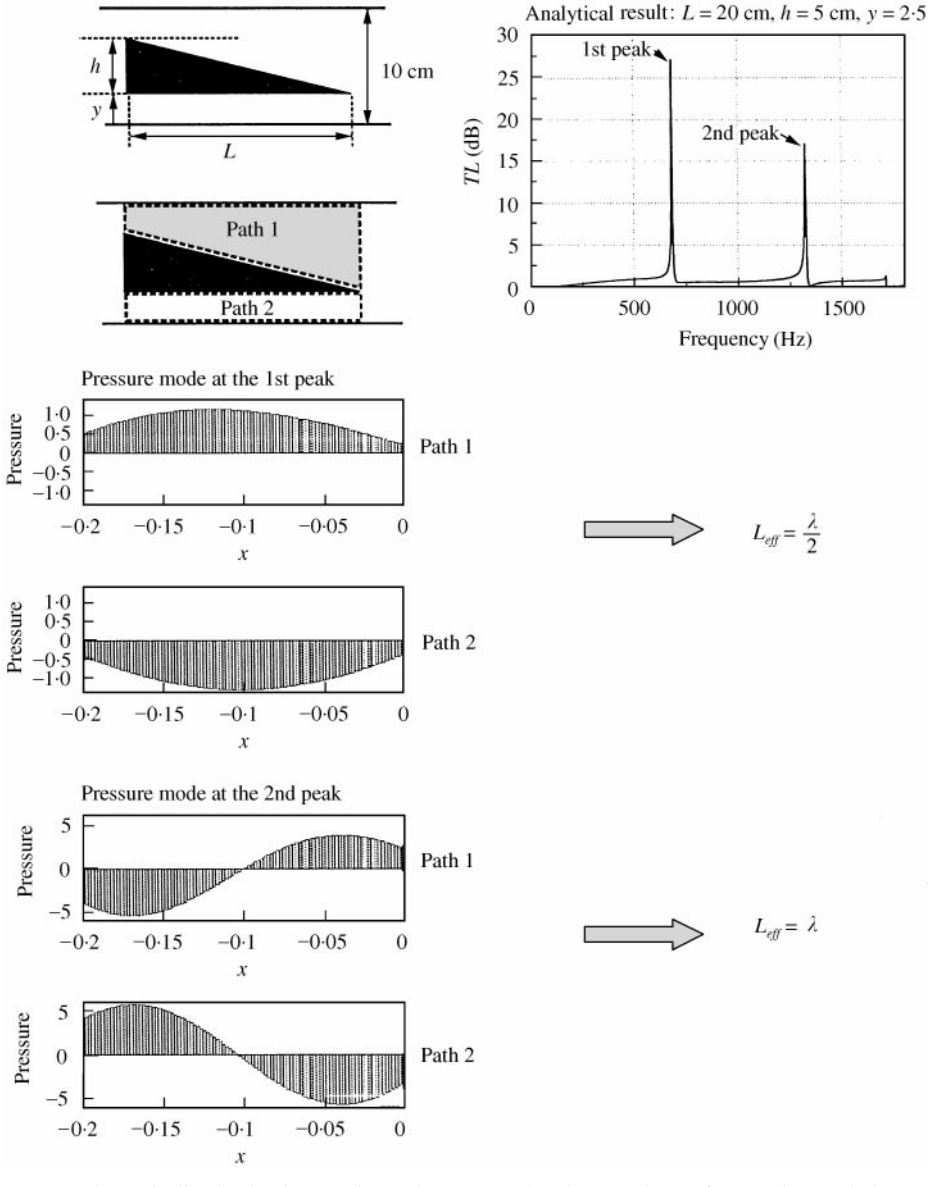

Figure 15. Theoretically obtained acoustic modes $|P| \times \cos(< P)$ at peak TL frequencies. P designates the acoustic pressure. Note that the acoustic modes in the two asymmetric paths are 180° out of phase.

screen height h. However, one should keep in mind that magnitude of attenuation is significantly influenced by h.

7. CONCLUSIONS

It has been found that when an acoustic screen is installed in a duct so as to form a section with two asymmetric paths, periodic narrowband sound attenuations are observed. Similar acoustical phenomena occur in the well-known Herschel–Quinke tubes, which can be

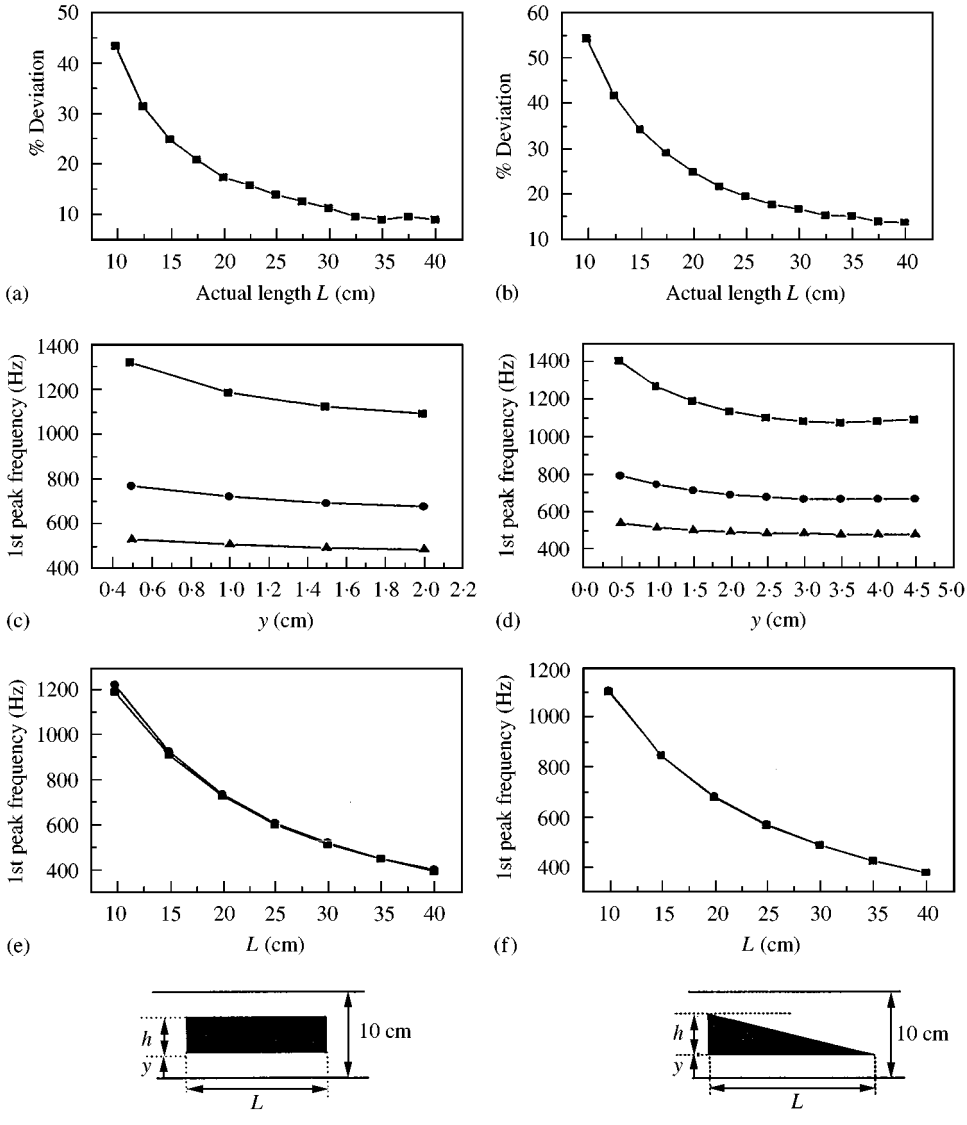

Figure 16. Parametric analysis. (a) %Deviation $= (L_{eff} - L)/L \times 100$; rectangular screen. (b) %Deviation $= (L_{eff} - L)/L \times 100$; wedge-shaped screen. (c) 1st peak frequency versus y with $h = 5$ cm; rectangular screen: —■— $L = 10$ cm; —●— $L = 20$ cm; —▲— $L = 30$ cm. (d) 1st peak frequency versus y with $h = 5$ cm; wedge-shaped screen: —■— $L = 10$ cm; —●— $L = 20$ cm; —▲— $L = 30$ cm. (e) 1st peak frequency versus h with $h = 1$ cm; rectangular screen: —●— $h = 3$ cm; —■— $h = 5$ cm. (f) 1st peak frequency versus h with $y = 2{\cdot}5$ cm; wedge-shaped screen: —■— $h = 3$ cm; —●— $h = 5$ cm.

explained by one-dimensional plane wave model. However, the noise attenuation studied in this paper is attributed to the non-propagating higher order modes that trigger longitudinal resonance along asymmetric paths. The analytical model in which the higher order mode effects had been taken into account showed very good agreement with the experimental and numerical results. It was found that the peak frequencies correspond to the longitudinal resonance frequencies at which the effective length of a screen equals the integer multiples of one-half wavelength: $L_{eff} = n\lambda/2$ $(n = 1, 2, \ldots)$. The 1st cross modes excited due to

asymmetric impedance distribution across the junctions were found to be responsible for the narrowband noise attenuation phenomenon.

The narrowband noise attenuation characteristics of acoustic screens revealed here can be applied in ventilation ducts where tonal noise components are dominant and space limitation is an issue. Yet, the effect of steady flow has not been taken into account in this paper. Future research on this subject would need to incorporate the effect of steady flow to fully assess its applicability to ventilation systems.

ACKNOWLEDGMENT

The authors would like to thank Professor D. A. Biesfer for his constructive advices in the revision of the manuscript. The research has been partly supported by KOSEF (Korean Science and Engineering Foundation).

REFERENCES

1. A. Cabelli 1980 *Journal of Sound and Vibration* **68**, 369–388. The acoustic characteristics of duct bend.
2. C. R. Fuller and D. A. Bies 1978 *Journal of Sound Vibration* **56**, 45–59. A reactive acoustic attenuator.
3. G. W. Stewart 1928 *Physics Review* **31**, 696–698. The theory of the Herschel–Quinke tube.
4. E. L. Hixson and J. V. Kahlbau 1963 *Journal of Acoustical Society of America* **35**, 1895. Quincke-tube acoustic filter for fluid ducts.
5. A. Selamet, N. S. Dickey and J. M. Novak 1994 *Journal of Acoustical Society of America* **96**, 3177–3185. The Herschell–Quinke tube: a theoretical, computational, and experimental investigation.
6. Zhu Zhichi, Li Song, Tian Rui, Guo Rui, Dai Genhua and Li Peizi 1998 *Noise Control Engineering Journal* **46**. Application of Quincke tubes to flow ducts as a sound attenuation device.
7. J. Y. Chung and D. A. Blaser 1980 *Journal of Acoustical Society of America* **68**, 907–921. Transfer function method of measuring in-duct acoustic properties. I. theory
8. A. D. Pierce 1994 *Acoustics*: *An Introduction to its Physical Principles and Applications* 360–362. New York. *The Acoustical Society of America.*
9. *E. Kreyszig* 1998 *Advanced Engineering Mathematics*, 205–213. New York: John Wiley & Sons.

APPENDIX A: DERIVATION OF $X_1(x, t)$ FROM THE WEBSTER HORN EQUATION

The cross-sectional area of Path 1 in Figure 11 can be expressed mathematically as

$$A(x) = B\left(W_1 - \frac{h}{L}x\right) = Bg(x), \tag{A1}$$

where B is the width of the duct and $g(x) = W_1 - (h/L)\,x$. From the Webster Horn equation which describes the wave propagation in Path 1 is

$$\frac{A(x)}{c^2}\frac{\partial^2 p}{\partial t^2} = \frac{\partial}{\partial x}\left\{A(x)\frac{\partial p}{\partial x}\right\}. \tag{A2}$$

Substituting of equation (A1) in equation (A2) and setting $p(x, t) = X_{P1}(x)\exp(\mathrm{i}\omega t)$, one can obtain the following ordinary differential equation:

$$\frac{\mathrm{d}^2 X_{P1}}{\mathrm{d}x^2} + \frac{1}{g(x)}\frac{\mathrm{d}g}{\mathrm{d}x}\frac{\mathrm{d}X_{P1}}{\mathrm{d}x} + k_0^2 X_{P1} = 0, \tag{A3}$$

where $k_0 = \omega/c$.

Substituting $g(x) = W_1 - (h/L)\,x$ in equation (A3), one can obtain

$$\frac{\mathrm{d}^2 X_{P1}}{\mathrm{d}x^2} + \frac{1}{x - (W_1 L/h)}\frac{\mathrm{d}X_{P1}}{\mathrm{d}x} + k_0^2 X_{P1} = 0. \tag{A4}$$

Let $\xi = -(x - W_1 L/h)$, then equation (A4) can be expressed in terms of ξ.

$$\frac{\mathrm{d}^2 X_{P1}}{\mathrm{d}\xi^2} + \frac{1}{\xi}\frac{\mathrm{d}X_{P1}}{\mathrm{d}\xi} + k_0^2 X_{P1} = 0. \tag{A5}$$

This is the Bessel equation [9] and its solution is

$$X_{P1} = \hat{C}_1 J_0(k\xi) + \hat{C}_2 Y_0(k\xi), \tag{A6}$$

where $\hat{C}_1$ and $\hat{C}_2$ are imaginary contants.
From $\xi = -(x - (W_1 L/h)$, equation (A6) can rewritten in terms x:

$$X_{P1} = \hat{C}_1 J_0\left[k_0\left(\frac{W_1 L}{h} - x\right)\right] + \hat{C}_2 Y_0\left[k_0\left(\frac{W_1 L}{h} - x\right)\right]. \tag{A7}$$

Thus, the plane wave propagation in Path 1 is described mathematically as

$$X_1(x, t) = p(x, t) = X_{P1}(x)\exp(\mathrm{i}\omega t),$$

$$X_1(x, t) = \left\{\hat{C}_1 J_0\left[k_0\left(\frac{W_1 L}{h} - x\right)\right] + \hat{C}_2 Y_0\left[k_0\left(\frac{W_1 L}{h} - x\right)\right]\right\}\exp(\mathrm{i}\omega t). \tag{A8}$$

APPENDIX B: ANALYTICAL MODELLING FOR RECTANGULAR SCREEN

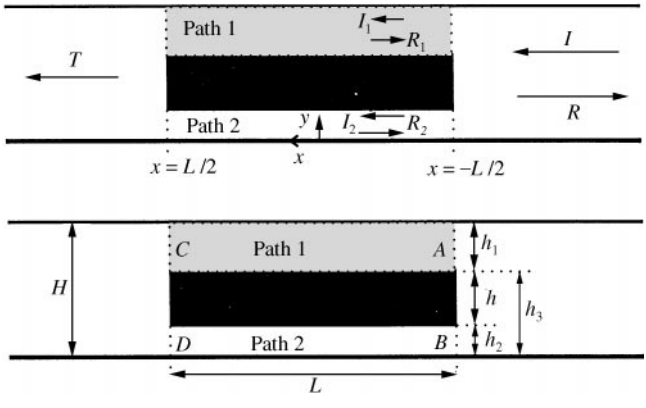

The duct system shown above can be divided into four sections. The upstream section, downstream section and the two divided paths.

The wave propagation in these sections can be described mathematically as follows:

$$I = \hat{P}_0^I \exp[\mathrm{i}(\omega t - k_0 x)], \qquad R = \sum_{m=0}^{n} \hat{P}_m^R \cos\left(m\pi\frac{y}{H}\right)\exp[\mathrm{i}(\omega t + k_m x)], \tag{B1, B2}$$

$$I_1 = \hat{I}_1 \exp[\mathrm{i}(\omega t - k_0 x)], \qquad R_1 = \hat{R}_1 \exp[\mathrm{i}(\omega t + k_0 x)], \tag{B3, B4}$$

$$I_2 = \hat{I}_2 \exp[\mathrm{i}(\omega t - k_0 x)], \qquad R_2 = \hat{R}_2 \exp[\mathrm{i}(\omega t + k_0 x)], \tag{B5, B6}$$

$$T = \sum_{m=0}^{n} \hat{P}_m^T \cos\left(m\pi \frac{y}{H}\right) \exp[\mathrm{i}(\omega t - k_m x)], \tag{B7}$$

where n is the number of modes considered in the reflected and transmitted wave. Recall that for a two-dimensional rectangular duct $(\omega/c)^2 = k^2 = k_x^2 + k_y^2$, where k_x designates the x-component wave number and k_y the y-component wave number. For rigid boundary condition, $k_m = k_x = \sqrt{(\omega/c)^2 - (m\pi/H)^2}$, where H is the duct height. To be strict, infinite number of modes ($n = \infty$) are generated at the discontinuities, but this is neither necessary nor practical as will be discussed later. Mean pressure is matched at junction A, B, C, and D, and tangential velocity continuity conditions are imposed at $x = \mathrm{L}/2$ and $x = -L/2$ just like what has been shown in section 5.1. The number of higher order modes was set equal to two ($n = 2$) for the same physical reasons given in section 5.1. With $n = 2$, one would be left with 10 equations and 11 unknown coefficients. Setting $\hat{P}_0^I = 1 + 0\mathrm{i}$ as a reference value, all the other coefficients can be found.